



Society of Petroleum Engineers

**SPE-195468-MS**

## **A New Multiphysics Method for Simultaneous Assessment of Hydrocarbon Saturation, Directional Permeability, and Saturation-Dependent Capillary Pressure**

Artur Posenato Garcia and Zoya Heidari, The University of Texas at Austin

Copyright 2019, Society of Petroleum Engineers

This paper was prepared for presentation at the SPE Europec featured at 81st EAGE Conference and Exhibition held in London, England, UK, 3-6 June 2019.

This paper was selected for presentation by an SPE program committee following review of information contained in an abstract submitted by the author(s). Contents of the paper have not been reviewed by the Society of Petroleum Engineers and are subject to correction by the author(s). The material does not necessarily reflect any position of the Society of Petroleum Engineers, its officers, or members. Electronic reproduction, distribution, or storage of any part of this paper without the written consent of the Society of Petroleum Engineers is prohibited. Permission to reproduce in print is restricted to an abstract of not more than 300 words; illustrations may not be copied. The abstract must contain conspicuous acknowledgment of SPE copyright.

---

### **Abstract**

Cost-effective exploitation of heterogeneous/anisotropic reservoirs (e.g., carbonate formations) reckons on accurate description of pore structure, dynamic petrophysical properties (e.g., directional permeability, saturation-dependent capillary pressure), and fluid distribution. However, techniques for reliable quantification of permeability and hydrocarbon saturation still rely on model calibration using core measurements. Furthermore, assessment of saturation-dependent capillary pressure has been limited to experimental measurements, such as mercury injection capillary pressure (MICP). The objectives of this paper include (a) developing a new multiphysics workflow to simultaneously quantify rock fabric features (e.g., porosity, tortuosity, and effective throat size) and hydrocarbon saturation from integrated interpretation of nuclear magnetic resonance (NMR) and electric measurements, (b) introducing rock physics models that incorporate the quantified rock fabric and partial water/hydrocarbon saturation for assessment of directional permeability and saturation-dependent capillary pressure, and (c) validating the reliability of the new workflow in pore- and core-scale domains.

To achieve these objectives, we introduce a new multiphysics workflow integrating NMR and electric measurements, honoring rock fabric, and minimizing calibration efforts. We estimate water saturation from the interpretation of dielectric measurements. Next, we develop a fluid substitution algorithm to estimate the  $T_2$  distribution corresponding to fully water-saturated rocks from the interpretation of NMR measurements. We use the estimated  $T_2$ -distribution for assessment of porosity, pore-size distribution, and effective pore-body size. Then, we develop a new physically meaningful resistivity model and apply it to obtain the constriction factor and, consequently, throat-size distribution from interpretation of resistivity measurements. Finally, throat-size distribution, porosity, and tortuosity are used to calculate directional permeability and saturation-dependent capillary pressure. We test the reliability of the new multiphysics workflow in core- and pore-scale domains on rock samples at different water saturation levels.

The introduced multiphysics workflow provides accurate description of the pore structure and fluid distribution in partially water-saturated formations with complex pore structure. Moreover, this new method enables real-time well-log-based assessment of saturation-dependent capillary pressure and directional permeability (in presence of directional electrical measurements) in reservoir conditions, which was not

possible before. Quantification of capillary pressure has been limited to measurements in laboratory conditions, where the differences in stress field reduce the accuracy of the estimates. We verified that the estimates of permeability, saturation-dependent capillary pressure, and throat-size distribution obtained from the application of the new workflow agreed with those experimentally determined from core samples. Finally, since the new workflow relies on fundamental rock physics principles, hydrocarbon saturation, permeability, and saturation-dependent capillary pressure can be estimated from well-logs with minimum calibration efforts, which is another unique contribution of this work.

## Introduction

Permeability assessment in carbonate formations can be challenging, especially in formations with complex morphology and pore structure. In these rocks, the application of conventional porosity-permeability correlations obtained from core-scale measurements (Nelson 1994) to log-scale measurements are likely to be inaccurate. The accuracy of permeability estimates can be significantly improved if the permeability correlations are developed in a class-by-class basis (Oyewole et al. 2016; Purba et al. 2018). However, these techniques still rely on calibrations performed either in the core- or pore-scale domains. Alternatively, rock-physics models for permeability assessment have been analytically derived based on simplified assumptions. Kozeny's (1927) equation is among the most notable models in this category. Kozeny (1927) assumed the pore network of a sedimentary rock could be approximated by a bundle of tortuous capillary tubes. Furthermore, Kozeny (1927) assumed that the Darcy flow regime in porous media corresponded to Stokes flow inside the bundle of capillary tubes. Under these assumptions, he analytically derived the following equation

$$k = \frac{r_H^2 \phi}{8\tau_H^2}, \quad (1)$$

where  $k$  is the permeability,  $r_H$  is the hydraulic radius of the capillary tubes,  $\phi$  is the porosity, and  $\tau_H$  is the hydraulic tortuosity. The tortuosity corresponds to the ratio of the tortuous length of the capillary tubes between two parallel planes where the hydraulic head difference is applied, divided by the distance between the planes (Clennell 1997; Garcia and Heidari 2018a), and is given by

$$\tau_H = \frac{L_e}{L}. \quad (2)$$

There are many available techniques for estimating porosity from petrophysical measurements such as neutron porosity, bulk density, acoustic logs, and nuclear magnetic resonance (NMR) measurements to name a few. However, estimating hydraulic radius and hydraulic tortuosity in a depth-by-depth basis from borehole geophysical measurements can be challenging. Furthermore, most of the petrophysical measurements available do not directly quantify hydraulic parameters.

There are petrophysical measurements that characterize physical phenomena which are analogous to the fluid flow in porous media. Hence, approximations to the hydraulic parameters can be obtained from the interpretation of these measurements. Several researchers have observed the similarities between the electric current flux and the Darcian fluid flow in porous media (Wyllie and Spangler 1952; Katz and Thompson 1987). The fluid flow and current flux are both controlled by diffusion mechanisms, but they are subject to different boundary conditions at the fluid-solid interface. On one hand, the fluid flow is subject to a no-slip boundary condition whereas on the other hand, the current flux is subject to a boundary condition of no-perpendicular current flux. Figure 1 illustrates a comparison between the fluid flow and the electric current flux in a conceptualized porous media represented by two spherical pores of different radii connected by a single throat. Figures 1a and 1b show the streamlines obtained from the numerical simulation of the fluid

flow using the single-phase single-component Lattice Boltzmann Method (Chen and Doolen 1998) and electric current flux problems solving Laplace's equation (Garcia and Heidari 2018a), respectively.

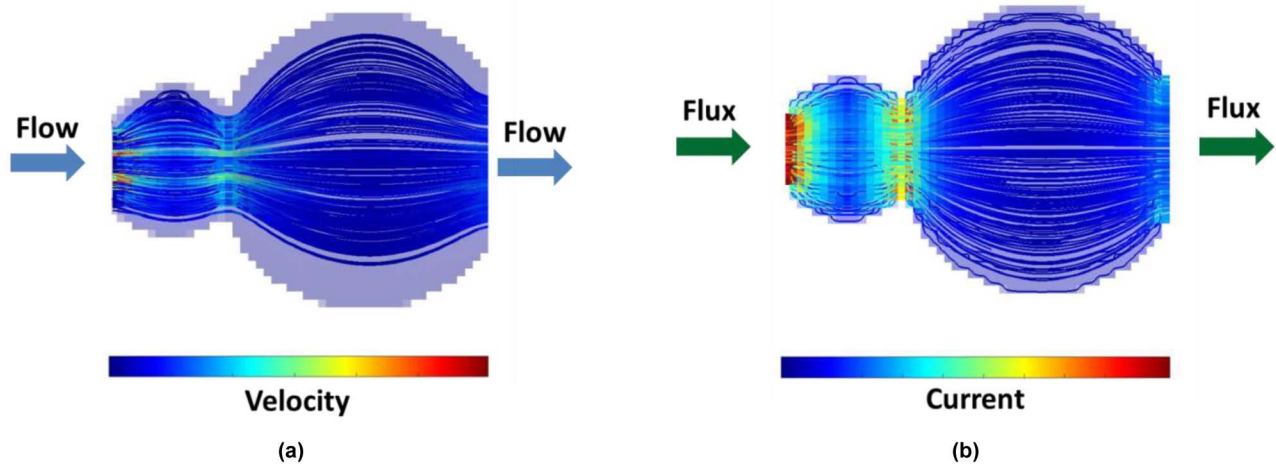


Figure 1—Comparison of the streamlines in a conceptual porous medium associated with (a) fluid flow simulated using single-component single-phase D3Q19 Lattice Boltzmann Method and (b) electric current flux simulated by solving Laplace's equation (Garcia and Heidari 2018a).

Even though the relationship between the diffusive problems of electric current flux and fluid flow in porous media has been well known, it was not until the work of Johnson et al. (1986) that this relationship has been rigorously established. Johnson et al. (1986) analytically derived a permeability equation incorporating information from resistivity measurements as

$$k = \frac{\Lambda^2}{8F}, \quad (3)$$

where  $F$  is the formation factor, defined as the resistivity of the rock, 100% saturated with water, divided by the resistivity of the brine (Archie 1942), and  $\Lambda$  is a parameter characteristic of the geometry of the porous media. Johnson et al. (1986) derived an expression for calculating precisely  $\Lambda$  as

$$\frac{2}{\Lambda} = \frac{\int |\nabla \Phi|^2 dS}{\int |\nabla \Phi|^2 dV}, \quad (4)$$

where  $\nabla \Phi$  is the gradient of electric potential,  $S$  is surface of the pores, and  $V$  is volume of the pores. However, the information about the electric potential distribution is not available in field cases, severely limiting the practical use of Equation 3.

Another permeability model incorporating fabric features as its inputs was analytically derived by Berg (2014). Under the assumption that the laminar fluid flow in porous media occurs through stream tubes of variable cross-sectional area, he proposed the following permeability equation

$$k = \frac{L_H^2 \phi_c}{8C_H \tau_H^2}, \quad (5)$$

where  $L_H$  is the characteristic hydraulic length,  $\phi_c$  is the connected porosity, and the hydraulic constriction factor,  $C_H$ , is defined as

$$C_H = \frac{1}{L^2} \int_0^L A^2(x) dx \int_0^L \frac{1}{A^2(x)} dx, \quad (6)$$

for a straight circular pore channel of length  $L$  with cross-sectional area  $A(x)$  at position  $x$ .

Once again, the rigorous application of Equation 5 requires a detailed knowledge of the pore structure, which is usually not available. Furthermore, it is not evident how to estimate the characteristic hydraulic length,  $L_H$ , in actual field cases. In order to address these issues, Garcia et al. (2018a) introduced a new permeability model, based on Equation 5, as

$$\langle k \rangle_{SM} = \frac{\phi_c}{8C_H \tau_H^2} \langle r_P^2 \rangle_{SM}, \quad (7)$$

where the characteristic hydraulic length squared,  $L_H^2$ , is replaced by the effective pore size squared,  $\langle r_P^2 \rangle_{SM}$ .

The effective pore is a statistical mean of the distribution of pore sizes squared obtained from the interpretation of NMR measurements. Fundamentally, the NMR  $T_2$  distribution is translated into pore-size distribution by assuming spherical pores (or other simple geometries) and, hence, the effective pore size can be calculated from

$$\langle r_P^2 \rangle_{SM} = \left\langle \left[ \frac{3\rho T_{2b} T_2}{T_{2b} - T_2} \right]^2 \right\rangle_{SM}, \quad (8)$$

where  $\rho$  is the surface relaxivity,  $T_{2b}$  is the bulk relaxation time,  $T_2$  corresponds to each value of transverse magnetization time, and  $SM$  stands for statistical mean. In particular, Garcia et al. (2018a) utilized the geometrical mean to the core-scale domain. Moreover, they assumed that the hydraulic constriction factor approximates the pore-to-throat size relationship via

$$C_H \cong \frac{\langle r_P^2 \rangle_{SM}}{\langle r_T^2 \rangle_{SM}}, \quad (9)$$

where  $\langle r_T^2 \rangle_{SM}$  corresponds to the effective throat size. It is interesting to note that, by substituting Equation 9 into Equation 7 we obtain

$$k = \frac{\langle r_T^2 \rangle_{SM} \phi}{8\tau_H^2}, \quad (10)$$

which is very similar to Kozeny's (1927) model given by Equation 1.

Garcia et al. (2018a) introduced a workflow to estimate all the rock fabric features required for permeability assessment (i.e., porosity, tortuosity, constriction factor, and effective pore size) directly from the interpretation of NMR, electrical conductivity, and dielectric permittivity measurements. This new workflow could be applied to estimate pore-throat size distribution, saturation dependent capillary pressure curves, and even directional permeability provided directional resistivity measurements are available. Furthermore, since it relied on fundamental rock-physics models with simplifying assumptions, the workflow could be directly applied to any fully-water-saturated and water-base-mud-invaded near-wellbore regions, completely eliminating calibration efforts. The main limitation in the previously introduced workflow for permeability assessment (Garcia et al. 2018a) is that it was conceived for fully water-saturated porous media. However, most of the practical applications in the petroleum industry correspond to formations partially saturated with hydrocarbon.

In order to address the aforementioned limitation, in this paper we introduce a new multiphysics workflow for permeability assessment by integrating NMR, dielectric permittivity, and electric resistivity

measurements performed on partially water-saturated rocks. The new workflow relies on fundamental rock-physics models honoring rock fabric, and thus minimizing calibration efforts.

## Method

In this section, we describe a new workflow to estimate permeability that integrates the interpretation of NMR, dielectric permittivity, and electrical conductivity measurements performed on partially water-saturated water-wet rocks. In order to estimate permeability while honoring rock fabric, it is necessary to estimate porosity, water saturation, tortuosity, and pore and pore-throat size. However, independently estimating each one of these parameters with minimum calibration efforts can be challenging. Porosity can be estimated via numerous approaches from available well-log measurements (e.g., neutron porosity and density measurements). In this paper, we estimate the water saturation from high-frequency (i.e., 960 MHz) dielectric-permittivity measurements by applying the Complex Refractive Index Model (CRIM) (Birchak et al. 1974). We assume that the geometric tortuosity can be estimated from a fully water-saturated zone by applying the concept of capacitive formation factor as a measure of pore structure (Bitterlich and Wobking 1970; Clennell 1997; Garcia et al. 2018a). Next, we perform fluid substitution to estimate the NMR  $T_2$  (transverse magnetization decay relaxation time) distribution of a fully-water saturated rock from NMR measurements performed on partially water-saturated rocks. The calculated  $T_2$  distribution translates into pore-size distribution. We define a new mechanistic function that relates the geometrical tortuosity to the electrical tortuosity and we apply it to calculate the constriction factor from electrical resistivity measurements. Finally, we estimate permeability, throat-size distribution, and saturation-dependent capillary pressure.

### Estimating Water Saturation

We estimate the water saturation from high-frequency (i.e., 960 MHz) dielectric permittivity measurements. At such frequency, the dielectric permittivity response of sedimentary rocks is dominantly volumetric with respect to the solids and grains. Consequently, the relationship between the wave propagation constant of the rock,  $\gamma_R^{wave}$ , and the wave propagation constants of the constituent elements of the rock is given by (Birchak et al. 1974; Hizem et al. 2008)

$$\gamma_R^{wave} = (1 - \phi) \gamma_g^{wave} + S_w \phi \gamma_w + (1 - S_w) \phi \gamma_{HC}^{wave}, \quad (11)$$

where  $S_w$  is the water saturation,  $\gamma_g^{wave}$  is the wave propagation constant on the grains,  $\gamma_w^{wave}$  is the wave propagation constant on the brine, and  $\gamma_{HC}^{wave}$  is the wave propagation constant on the hydrocarbon. The wave propagation,  $\gamma^{wave}$ , is a complex number and it is related to the complex dielectric permittivity,  $\epsilon^*$ , via

$$\gamma^{wave} = j\omega\sqrt{\mu_0\epsilon_0}\sqrt{\epsilon^*}, \quad (12)$$

where  $j$  is the imaginary number ( $j^2 = -1$ ),  $\omega$  is the angular frequency (rad/s),  $\mu_0$  is the magnetic permeability of the free space ( $4\pi \times 10^{-7}$  H/m), and  $\epsilon_0$  is the dielectric permittivity of the free space ( $8.854 \times 10^{-12}$  F/m). By substituting Equation 12 into Equation 11, we obtain the CRIM (Birchak et al. 1974) as

$$\sqrt{\epsilon_R} = (1 - \phi) \sqrt{\epsilon_g} + S_w \phi \sqrt{\epsilon_w} + (1 - S_w) \phi \sqrt{\epsilon_{HC}}, \quad (13)$$

where  $\epsilon_R$  is the dielectric permittivity of the rock,  $\epsilon_g$  is the dielectric permittivity of the grain,  $\epsilon_w$  is the dielectric permittivity of the brine, and  $\epsilon_{HC}$  is the dielectric permittivity of the hydrocarbon are all complex quantities. The water saturation,  $S_w$ , is estimated from Equation 13.



### Estimating Constriction Factor

The interpretation of electrical resistivity measurements is usually performed with the objective of estimating hydrocarbon/water saturation. However, in this paper we utilize the information contained in electrical resistivity measurements to estimate the constriction factor. For this purpose, we employ the resistivity equation introduced by [Garcia and Heidari \(2018a\)](#), which extends [Berg's \(2012\)](#) resistivity equation to partially water-saturated rocks via

$$\frac{\sigma_R}{\sigma_w} = \frac{1}{C_e} \frac{\phi_c S_w}{\tau_e^2}, \quad (14)$$

where  $C_e$  is the electrical constriction factor,  $\phi_c$  is the connected porosity, and  $\tau_e$  is the electrical tortuosity. We assume that the electrical constriction factor is approximately constant (independent of the water saturation) and that it provides a good approximation to the hydraulic constriction factor,  $C_H$ . The electrical tortuosity, on the other hand, depends on the water saturation in a complex way. In order to minimize the calibration efforts required for the interpretation of electrical measurements, we assumed a simple geometry (water-wet spherical pores saturated by water with a constant thickness of water on the grain surface) from which the dependence of  $\tau_e$  to  $S_w$  is given by

$$\tau_e = \tau_g \left[ 1 + \left[ \frac{(\pi - 2\gamma)}{2 \cos(\gamma)} - 1 \right] (1 - S_w)^{\frac{1}{3}} \right], \quad (15)$$

where  $\gamma$  is a function of the pore and throat geometries, as discussed in more detail in Appendix A. [Equation 14](#) is then solved numerically to estimate  $C_e$ , where the inputs are the geometric tortuosity ( $\tau_g$ ), the water saturation ( $S_w$ ), and the connected porosity ( $\phi_c$ ). The total and connected porosities are approximately equal in the rock samples documented in this paper. These two porosity values might be significantly different in formations with more complex pore structures. We also assume that  $\tau_g$  can be obtained either from the interpretation of dielectric permittivity measurements in a fully water-saturated zone with the same rock type ([Bitterlich and Wobking 1970](#); [Garcia et al. 2018a](#)) or from numerical simulations performed on pore-scale images.

### NMR Fluid Substitution and Assessment of Pore-Size Distribution in Partially-Saturated Rocks

The interpretation of NMR measurements performed on fully water-saturated rocks can be used for permeability assessment and to estimate pore-size distribution ([Arns 2004](#)). However, most borehole measurements are performed on sedimentary rocks partially saturated with hydrocarbons, significantly affecting both the longitudinal and transverse magnetization decay times. Consequently, in order to incorporate the interpretation of NMR measurements in permeability assessment workflows, it is necessary to replace the hydrocarbon response of the original measurement with an equivalent water response ([Medellin et al. 2019a](#)). Several fluid substitution techniques have been recently introduced ([Christensen et al. 2015](#); [Minh et al. 2016](#); [Medellin et al. 2019a, 2019b](#)).

In this paper, we propose a two-step NMR fluid substitution method for water-wet rocks partially saturated with hydrocarbons. In the first step, we remove the NMR response due to the bulk relaxation of hydrocarbon. [Figure 2a](#) illustrates the  $T_2$  distribution of a water-wet partially hydrocarbon-saturated rock where the  $T_2$  distribution is divided into water (blue) and hydrocarbon (red) components. In such case, where the contribution of hydrocarbon to the  $T_2$  distribution can be clearly identified, the  $T_2$  distribution of the water-saturated region can be obtained by simply eliminating the hydrocarbon contribution. Alternatively, if the contribution of hydrocarbon is not easily identifiable from the  $T_2$  distribution, in cases where the hydrocarbon and water transverse relaxation times overlap, we can apply [Equation B16](#) to estimate the transverse magnetization decay of the water-saturated volume,  $M_w$ . Then, the  $T_2$  distribution of the water-

saturated region can be calculated directly from  $M_w$ . In order to apply Equation B16, we need to measure the transverse magnetization decay of the hydrocarbon phase alone, which can be easily done in the laboratory if a representative hydrocarbon sample is available.

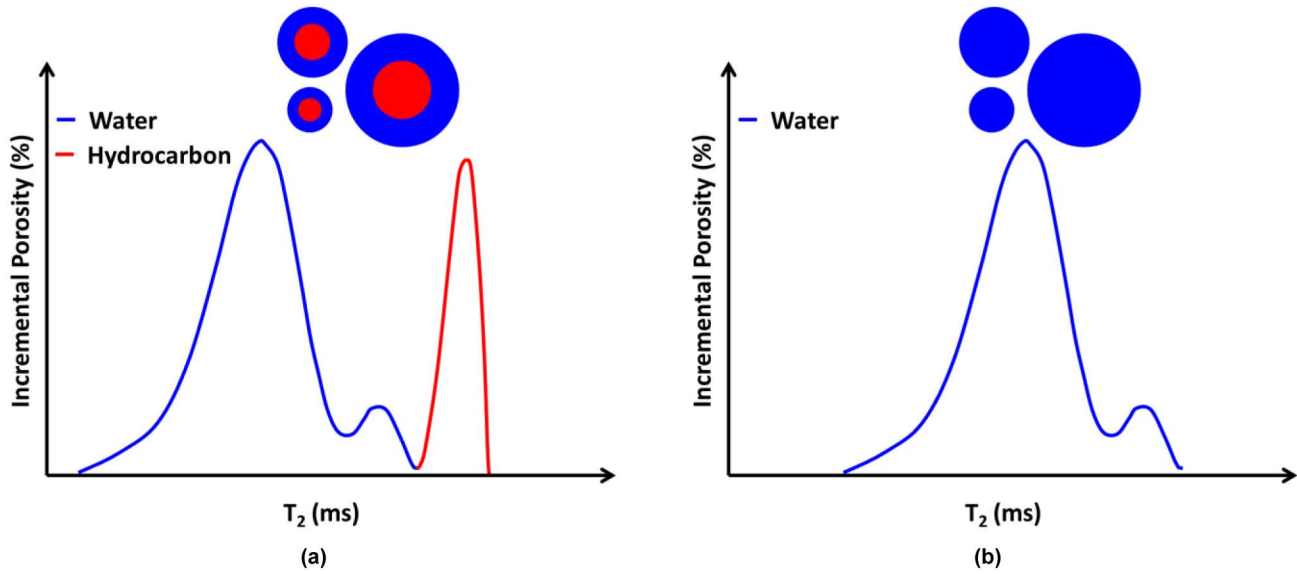


Figure 2—Illustration of  $T_2$  distributions before and after the application of the NMR fluid substitution method: (a)  $T_2$  distribution of the partially hydrocarbon-saturated rock where the contribution of water and hydrocarbon are illustrated in blue and red, respectively, and (b) the equivalent  $T_2$  distribution of a fully water-saturated rock.

The second step of the NMR fluid substitution method consists of converting the  $T_2$  distribution of the water-saturated region into a  $T_2$  distribution of a fully water-saturated rock. This step is accomplished via

$$T_{2@S_w=1} = \frac{T_{2b,w} T_{2@S_w \neq 1}}{S_w T_{2b,w} + (1 - S_w) T_{2@S_w \neq 1}}, \quad (16)$$

where  $T_{2@S_w=1}$  corresponds to the  $T_2$  values of a fully water-saturated rock,  $T_{2@S_w \neq 1}$  corresponds to the  $T_2$  values of water-saturated region, and  $T_{2b,w}$  is the bulk relaxation time of the pure brine. Equation 16 is derived in Appendix B by assuming that the NMR response takes place in the fast diffusion regime, the pores are diffusionally decoupled, there is no relaxation at the water-hydrocarbon interface, and the contribution of internal field gradient to the relaxation is negligible.

The equivalent  $T_2$  distribution corresponding to a fully water-saturated rock can be translated into pore-size distribution through

$$r_p = \frac{3\rho T_{2b,w} T_{2@S_w=1}}{T_{2b,w} - T_{2@S_w=1}}, \quad (17)$$

where each value  $T_{2@S_w=1}$  is associated with an individual pore size  $r_p$ . Then, the pore-size distribution can be converted to effective pore size through Equation 8. Equation 8 is nothing more than the statistical mean of Equation 17 squared. Equations 8 and 17 have been derived in Appendix B under the assumption that the pores are spherical, from which we can determine the surface-to-volume ratio, and additionally the same assumptions required for the derivation of Equation 16. Equations 16 and 17 can be further simplified by assuming that the bulk relaxation time of the pure brine is much larger than the  $T_2$  values due to the surface relaxation. However, Equations 16 and 17 are already simple enough so that such simplifications are not required unless the bulk relaxation time of brine is not known accurately.

### Assessment of Throat-Size Distribution and Saturation-Dependent Capillary Pressure

The pore-size distribution obtained from Equation 17 can be translated into pore-throat-size distribution via

$$r_T = \frac{r_p}{\sqrt{C_H}}, \quad (18)$$

where  $C_H$  is the hydraulic constriction factor and, in this paper, it is assumed to be constant for the entire pore network. Furthermore, it is approximated by the electrical constriction factor obtained from the interpretation of electrical resistivity measurements using Equation 14. Similarly, the effective throat size can be calculated from the statistical mean of Equation 18 squared or, equivalently, from Equation 9. Next, we calculate the permeability of the formation using Equation 10.

Furthermore, the throat-size distribution can be translated into saturation-dependent capillary pressure via (Washburn 1921)

$$P_C = \frac{2\gamma^{ST}}{r_T} \cos \theta, \quad (19)$$

where for each pore-throat radius (for a cylindrical pore geometry),  $r_T$ , there is a corresponding capillary pressure,  $P_C$ ,  $\gamma^{ST}$  is the surface tension of the saturating fluid, and  $\theta$  is the corresponding contact angle in air. In this paper, we assume the interfacial tension of mercury of 480 dynes/cm<sup>2</sup> (Adamson and Gast 1997; Müller-Huber et al. 2018) to be able to compare the results obtained from Equation 18 to those obtained from MICP measurements.

### Workflow for Model Application

Figure 3 illustrates the proposed workflow to simultaneously quantify rock fabric features and hydrocarbon saturation from integrated interpretation of nuclear magnetic resonance (NMR) and electric measurements.

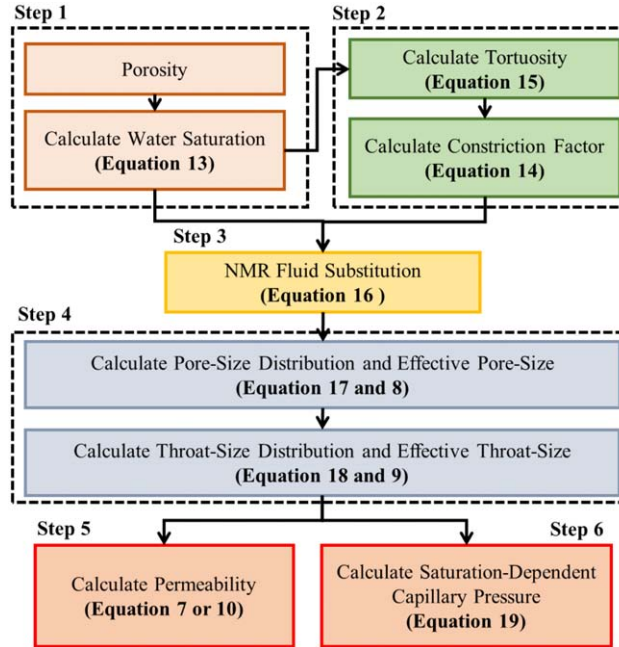


Figure 3—The proposed workflow for estimating permeability, electrical tortuosity, constriction factor, pore-throat-size distribution, and saturation-dependent capillary pressure through joint interpretation of NMR, dielectric permittivity, and resistivity measurements.

The application of the proposed model to a given formation requires a sequence of steps detailed below:



1. Estimate the porosity from the interpretation of neutron porosity, density, and/or acoustic logs in field applications, gravimetric methods in core applications, and image analysis in the pore-scale domain. Then, estimate the water saturation from the interpretation of dielectric permittivity measurements performed at 960 MHz from Equation 13. The inputs to Equation 13 are the porosity, the dielectric permittivity of the brine at 960 MHz, the dielectric permittivity of the hydrocarbon, the dielectric permittivity of the grains, and the experimentally measured dielectric permittivity of the saturated rock.
2. Estimate the geometric tortuosity from the interpretation of dielectric permittivity measurements performed in a fully water-saturated zone using Bitterlich and Wobking (1970) capacitive formation factor equation. Then, calculate the constriction factor from Equation 14. The inputs to Equation 14 are the porosity, the water saturation, the electrical tortuosity (Equation 15), the electrical conductivity of the brine, and the experimentally measured electrical conductivity of the saturated rock.
3. Apply the introduced NMR fluid substitution method to estimate the  $T_2$  distribution corresponding to a fully water-saturated rock. This is a two-step method: (1) obtain the  $T_2$  distribution of the water-saturated region by eliminating the hydrocarbon contribution to the  $T_2$  distribution (or equivalently to the transverse magnetization decay) and (2) convert the  $T_2$  distribution of the water-saturated region into a  $T_2$  distribution of a fully water-saturated rock through Equation 16. The inputs to Equation 16 are the  $T_2$  distributions of the water saturated region, the water saturation, and the bulk relaxation time of the brine.
4. Calculate the pore-size distribution and the effective pore size from Equations 17 and 8, respectively. The inputs to Equations 8 and 17 are the surface relaxivity of the pores, the  $T_2$  distribution of a fully water-saturated rock, and the bulk relaxation time of the brine. Then, calculate the pore-throat-size distribution and the effective pore-throat size from Equations 18 and 9, respectively. The inputs to Equations 9 and 18 are the pore-size distribution and the constriction factor.
5. Calculate the permeability from Equation 7 or, equivalently, from Equation 10. The inputs to Equation 7 are the porosity estimated in step 1, tortuosity and constriction factor estimated in step 2, and the effective pore size estimated in step 4. The inputs to Equation 10 are the porosity estimated in step 1, the tortuosity estimated in step 2, and the effective throat size estimated in step 4.
6. Calculate the saturation-dependent capillary pressure from Equation 19. The inputs to Equation 19 are pore-throat size distribution, the surface tension of the fluid, and the corresponding contact angle in air.

## Strategies for Model Verification

We tested the proposed workflow, illustrated in Figure 3, in the pore- and core-scale domains, as described in the following subsections. In the pore-scale domain, we verified the reliability of the introduced workflow using three-dimensional (3D) pore-scale images. These images were selected from a carbonate formation with complex pore structure. We synthetically saturated the pore-scale samples using the octagonal distance transform algorithm described by Garcia and Heidari (2018a) (Rosenfeld and Pfaltz 1968). Then, we performed numerical simulations on the 3D pore-scale images to obtain the inputs to the introduced workflow (i.e., NMR transverse magnetization decay, dielectric permittivity, and electric resistivity). Finally, we estimated permeability values through the introduced workflow and compared them against the results obtained from numerical simulation of fluid flow using Palabos (2013), an open-source Lattice Boltzmann Method (LBM) solver. Next, we tested the introduced workflow in the core-scale domain using Texas Cream Limestone samples. We first prepared the core samples with varying levels of water saturation. At each saturation level, we performed NMR, dielectric permittivity, and electric resistivity measurements

on the core samples. We estimated the permeability, throat-size distribution, and saturation-dependent capillary pressures using the introduced workflow (Figure 3). Then, we compared the estimates against the results obtained from a core flood setup and MICP measurements. The workflow for model verification is illustrated in Figure 4.

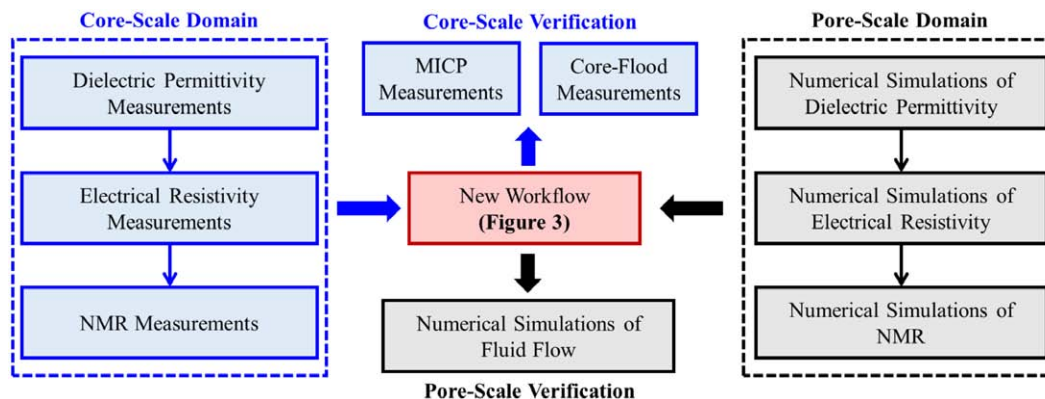


**Figure 4—Model verification process.** The verification process includes the dielectric permittivity, electrical resistivity, and NMR measurements as inputs to the introduced workflow, and MICP, core-flood measurements, and numerical simulations for the verification purpose.

### Sample Preparation and Alteration of Water-Saturation

First, we weigh the core samples using a PB303-S/FACT DeltaRange Mettler Toledo balance. The initial weight accounts for the solid grains and the moisture contained in the sample. Then, we place the samples in a Quincy Lab Inc Model 30 Lab Oven at 75 °C to remove the moisture. We take the samples from the oven every 24 hours, weigh them, and place them back into the oven. This procedure is repeated until no weight variation is observed indicating that the moisture has been removed. Afterwards, we place the core samples in −14 psi vacuum for 8 hours. The vacuum is generated by a Duoseal R 1420 Welch Vacuum Pump. Then, we use the vacuum pressure to inject a 2 wt% KCl brine into the core samples. Finally, we place the beakers containing the saturated samples covered with brine in a −14 psi vacuum for 30 minutes to minimize residual air dissolved in the brine. We change the water saturation on the core sample through the experimental workflow described by [Newgord et al. \(2018\)](#) including spontaneous (Amott cell) and forced (centrifuge) imbibition of brine and decane using a Beckman L8-M Ultracentrifuge.

### Permeability Assessment

The core flood experiment consisted of injecting brine with a constant flow rate through the core sample and measuring the pressure drop across the sample, with a confining pressure of 1,000 psi to the core samples. The setup included an ISCO series LC-2600 pump and Rosemount pressure transducer connected to a computer running National Instruments LabVIEW. We followed the procedure described by [Garcia et al. \(2018a\)](#).

### Dielectric Permittivity Measurements

We measure the dielectric permittivity of the core samples using a Keysight E5071C network analyzer. The measurements reported in this document require a simple terminated coaxial probe, Keysight N1501A, which is placed on top of the samples. We place the saturated rock samples (1.5"×1.5" or 1.5"×2") in contact with the coaxial probe with a constant pressure to enforce the best contact between the sample and the probe. Then, we measure the real part of the dielectric permittivity in the frequency range of 20 MHz to 1 GHz. We repeat the measurements several times on both sides of the sample to ensure that the roughness of the surface of the samples is not affecting the quality of the measurements.

## NMR Measurements

We measure the relaxation time of the transverse magnetization decay ( $T_2$ ) using a 2 MHz Magritek NMR Rock Core Analyzer with a Carr, Purcell, Meiboom and Gill (CPMG) pulse sequence. We set the inter-experiment delay to be 5 s, the minimum signal-to-noise ratio (SNR) to be 200, and the echo spacing time to be 100  $\mu$ s. Then, we measure the NMR  $T_2$  distribution of each fully brine-saturated core sample. NMR measurements are also performed to control the quality of the resistivity and dielectric permittivity measurements. We measure the  $T_2$  distribution before and after electrical measurements to verify that brine evaporation was negligible during the experiments.

## Resistivity Measurements

In this research, we use a two-terminal setup of a multi-frequency impedance analyzer (MFIA) from Zurich Instruments to measure the complex impedance of the rock samples. The core samples are placed in a core holder with wing nuts that are tightened along a threaded rod. The wing nuts are responsible for applying a pressure on the two end faces of core sample and maintaining a solid contact. The two metallic electrodes of the core holder are connected to the MFIA. A sinusoidal voltage excitation in the frequency range of 10 Hz to 500 kHz with an amplitude of 300 mV is applied to the core samples. We record the complex impedance and calculate the conductivity of the samples from the resistance measured at the minimum phase.

## MICP Measurements

We perform the mercury porosimetry analysis using a Micromeritics AutoPore IV 9500 Series. Mercury is injected into the rocks under controlled pressures ranging from 0 to 50,000 psi, allowing assessment of pore-throat-size distribution ranging from 0.005 to 300  $\mu$ m. Besides the pore-throat-size distribution, the MICP measurements provide saturation-dependent capillary pressure, total pore volume, total pore surface area, median pore diameter, and sample density.

## Results

In this section, we document the results obtained from testing the proposed workflow to estimate permeability and pore-throat-size distribution in the pore- and core-scale domains. To verify the workflow in pore-scale domain, we selected a pore-scale image from Happy Spraberry formation with a pixel resolution of 3.46  $\mu$ m and size of 600  $\times$  600  $\times$  900 voxels. Then, we segmented the micro-CT image into black and gray regions representing pores and grains, respectively, using Fiji ImageJ (Schindelin et al. 2012), an open-source image processing software. The resulting segmented pore-scale image from Happy Spraberry formation is illustrated in Figure 5a. To verify the workflow in the core-scale domain, we selected core samples from Texas Cream limestone (1.5  $\times$  1.5 in), as illustrated in Figure 5b.

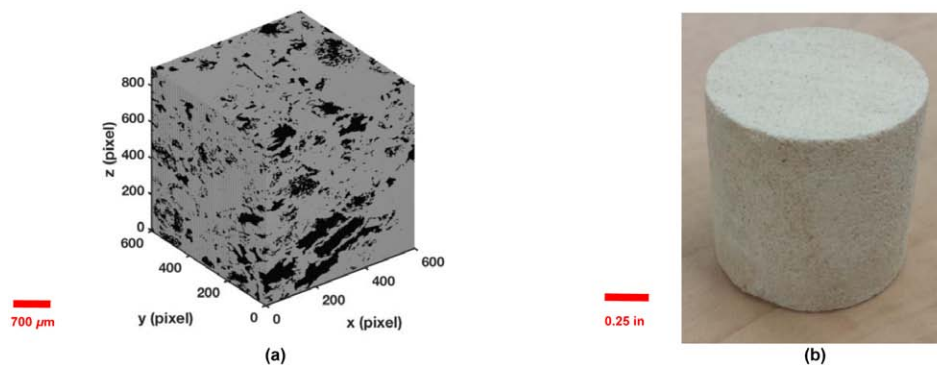


Figure 5—Samples used for the verification of the introduced workflow in the (a) pore-scale domain (Happy Spraberry formation) and (b) core-scale domain (Texas Cream limestone).

The 3D pore-scale binary image was divided into samples with  $300^3$  voxels and then we synthetically saturated the pore-scale samples using the octagonal distance transform algorithm described by Garcia and Heidari (2018a) (Rosenfeld and Pfaltz 1968). We obtained different levels of water saturation on the core sample after following the experimental workflow described by Newgord et al. (2018), including spontaneous (Amott cell) and forced (centrifuge) imbibitions of brine and decane.

### Step 1: Water Saturation Assessment

We applied the numerical simulator developed by Garcia and Heidari (2018b) to calculate the dielectric-permittivity response from pore-scale images at frequencies of 22, 100, 350 MHz, and 960 MHz. These frequencies correspond to the typical dielectric-dispersion log operation frequencies (Claverie 2012). In all dielectric permittivity and electrical conductivity simulations, we assumed that the pore space is filled with decane and 2 wt% NaCl brine at 25°C. The electrical properties of water are calculated using Stogryn's (1971) model, resulting in an electrical conductivity of 3.21 S/m and a relative dielectric permittivity of 71 at 960 MHz. Figure 6a shows an example of a simulated dielectric permittivity for a representative sample from Happy Spraberry formation at a water saturation of 46%. The core samples were saturated with decane and 2 wt% KCl brine. The electrical conductivity and dielectric permittivity of the brine at 25°C were experimentally determined to be 2.69 S/m and 60, respectively. Figure 6b shows an example of an experimentally measured dielectric permittivity in core sample from Texas Cream limestone formation at a water saturation of 49%.

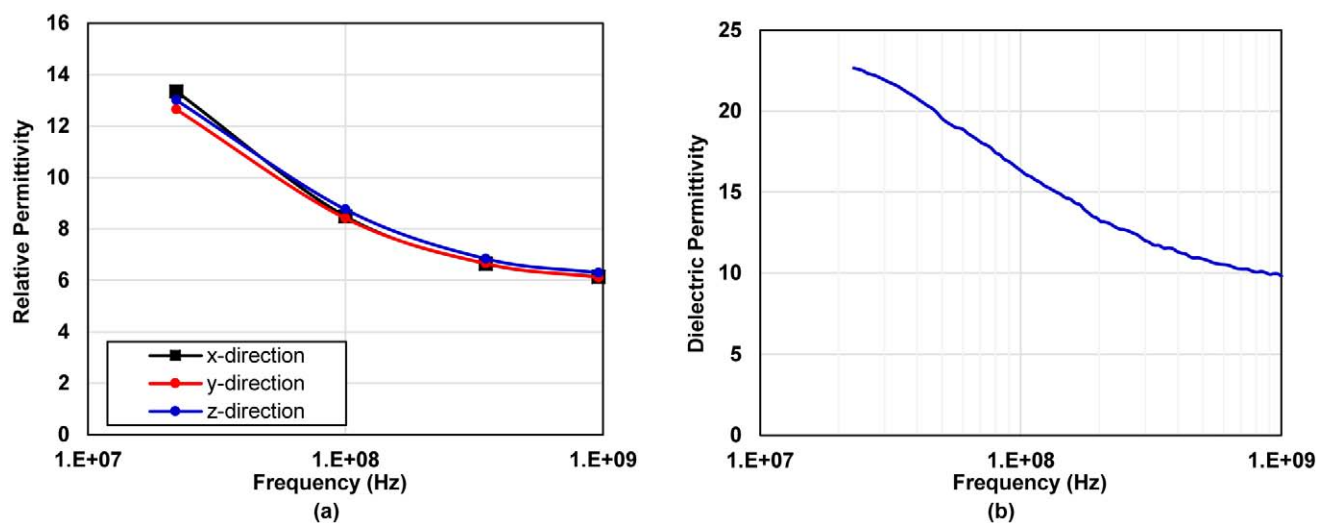


Figure 6—Dielectric permittivity obtained from (a) numerical simulations on a pore-scale image from Happy Spraberry formation ( $S_w = 46\%$ ) and (b) laboratory measurements performed on a core sample from Texas Cream limestone formation ( $S_w = 49\%$ ).

The actual saturations in the pore- and in the core-scale domains ranged from 43.8% to 84.2% and from 41.6% to 60.1%, respectively. The average relative error in water saturation estimates was less than 42% for all samples, in the pore- and core-scale domain. This level of uncertainty in water saturation assessment indicates that there is still room for improvement in the interpretation of dielectric permittivity measurements as documented in previous publications (Chen and Heidari 2014). In the subsequent steps we will assume that the water saturation is known and remove its uncertainty from the permeability estimates.

### Step 2: Assessment of Electrical Tortuosity and Constriction Factor

In this paper, we assumed that the geometric tortuosity can be obtained from the interpretation of permittivity measurements in a fully water-saturated zone (Bitterlich and Wobking 1970; Clennell 1997; Garcia et al. 2018a). The geometrical tortuosity was assumed to be 1.17 for the pore-scale 3D rock images from Happy



Spraberry formation (Garcia et al. 2018a, 2018b). We assumed 1.36 for the core sample from Texas Cream limestone formation, the average value reported by Garcia et al. (2018a) for all Texas Cream limestone samples. We estimated the constriction factor of all the pore-scale samples from Happy Spraberry formation to range from 7 to 108, which is within the range of values reported by Garcia et al. (2018a) for the fully water-saturated samples. For the sample from Texas Cream limestone formation, we estimated the constriction factor to be 2.46, which is also consistent with the values reported by Garcia et al. (2018a) for the fully water-saturated samples.

### Step 3: NMR Fluid Distribution

To calculate the transverse magnetization decay in each partially water-saturated pore-scale 3D image, we expanded the random-walk algorithm developed by Garcia et al. (2018a) to perform two-phase NMR magnetization decay simulations. We assumed bulk relaxation time, diffusion coefficient, and surface relaxivity of 3 s,  $2.0 \times 10^{-9} \text{ m}^2/\text{s}$ , and  $5.0 \times 10^{-6} \text{ m/s}$ , respectively, for the water phase, and of 1.1 s,  $0.67 \times 10^{-9} \text{ m}^2/\text{s}$ , and  $1.65 \times 10^{-6} \text{ m/s}$ , respectively, for the hydrocarbon phase. We initially assigned at least one walker per every four voxels in the pore space. The magnetization decay of the partially water-saturated rock was then calculated using Equation B16. Then, we applied a curvature-smoothing regularization algorithm to estimate the  $T_2$  distribution.

### Step 4: Assessment of Pore- and Throat-Size Distribution

Next, we estimated the pore- and throat-size distributions from the Equations 17 and 18, respectively. Figure 7a illustrates an example of pore- and throat-size distribution estimated by applying the new workflow in the pore-scale domain to a representative sample from Happy Spraberry formation at water saturation of 46%. The effective throat sizes estimated for the Happy Spraberry pore-scale 3D rock images ranged from 1.32 to  $7.60 \mu\text{m}$ . Garcia et al. (2018a) reported the effective throat sizes for the Happy Spraberry pore-scale 3D rock images ranging from 0.35 to  $9.82 \mu\text{m}$ , which are consistent with the results obtained in this paper.

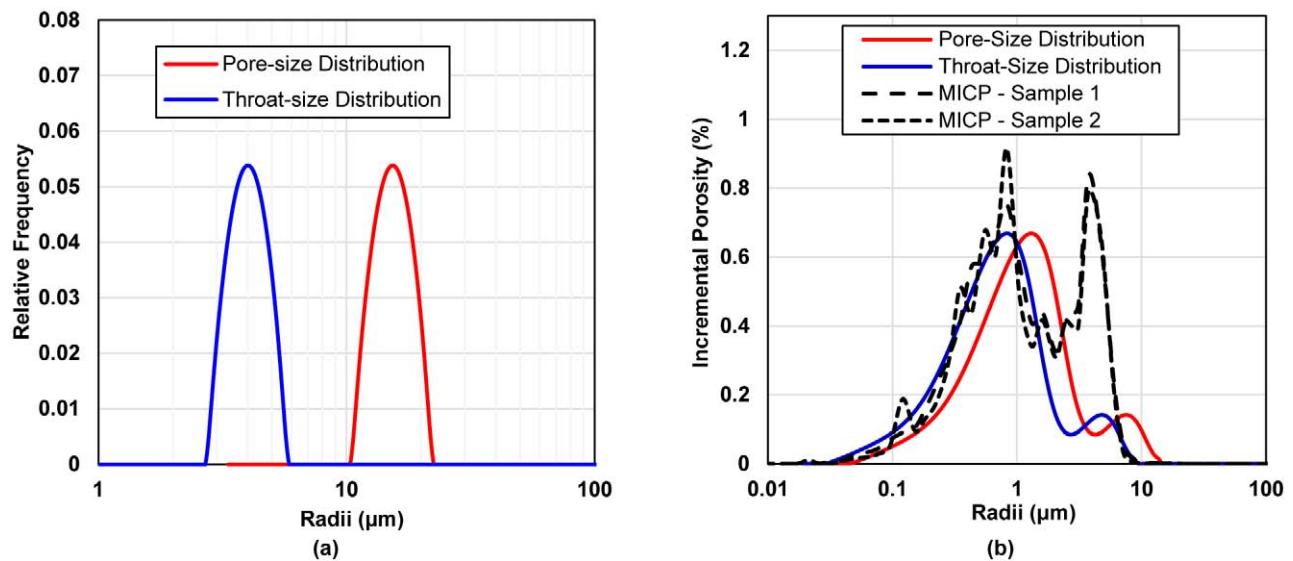


Figure 7—Comparison of pore- and throat-size distribution estimated from the application of the new workflow to (a) a representative sample from Happy Spraberry formation in the pore-scale domain and (b) a Texas Cream limestone sample in the core-scale domain, in addition to the corresponding results obtained from MICP measurements.

Figure 7b illustrates an example of pore- and throat-size distribution estimated by applying the new workflow in the core-scale domain on a core sample from Texas Cream limestone formation at water saturation of 49%. Furthermore, Figure 15b shows the comparison of the pore-throat size distribution obtained from MICP measurements performed on two Texas Cream limestone samples. These results



demonstrate that the estimated pore-throat size distribution is in excellent agreement with the results obtained from MICP measurements, in the core-scale domain.

### Step 5: Permeability Assessment

We estimated the directional permeability in the pore-scale domain through Equation 7. According to Garcia et al. (2018a), in the pore-scale domain, the harmonic mean provides more realistic results to the effective pore size calculated through Equation 8. They suggest that this is due to the fact that pore-scale images only map a small fraction of the rock and the number of parallel flow pathways is limited. Figure 8a illustrates the comparison between estimated and actual directional permeability for the set of pore-scale samples from the Happy Spraberry formation in the x-, y-, and z-directions. The average relative error in directional-permeability estimates obtained for all the subsamples is less than 145%, 116%, and 70% in the x-, y-, and z-directions, respectively. Then, we also estimated the permeability in the core-scale domain through Equation 7. In the core-scale domain, however, the geometric mean is a more reliable option for estimating the effective pore-size from Equation 8. According to Garcia et al. (2018a), this is because core samples map a larger fraction of the formation as compared to the pore-scale rock images. Consequently, there is a higher number of parallel flow pathways in the core-scale applications. Figure 8b illustrates the comparison between estimated and actual permeability for core sample from Texas Cream limestone formation, with an average relative error less than 28%.

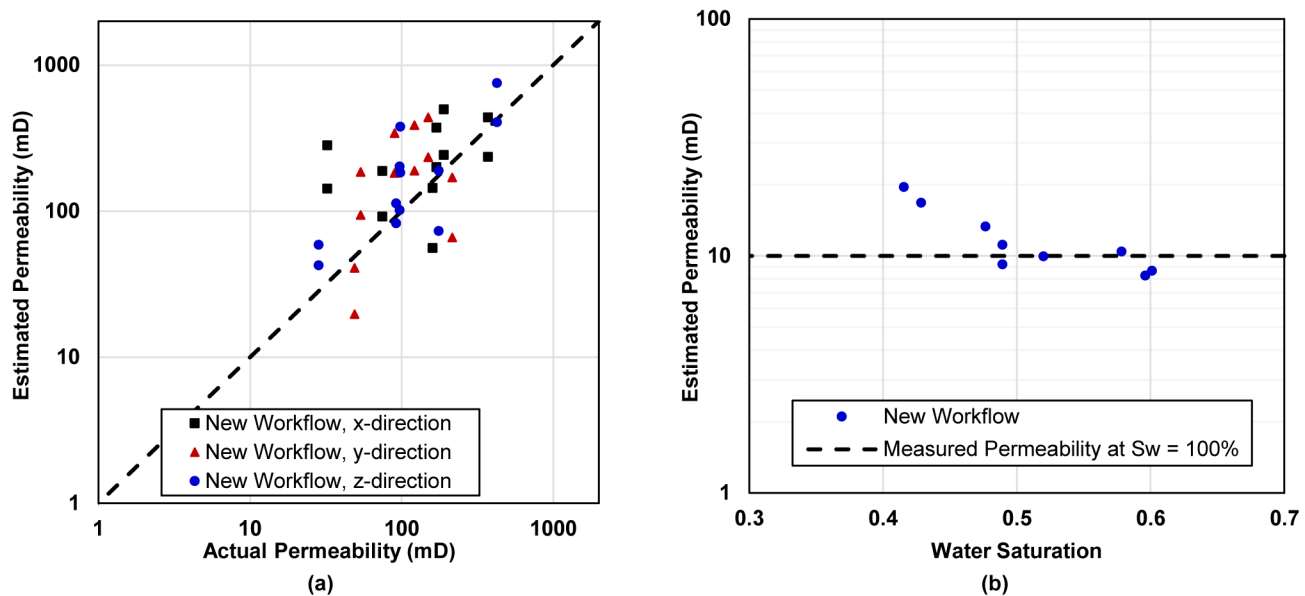


Figure 8—Comparison of (a) the pore-scale directional-permeability estimates using the new workflow (black circles for x-direction, red squares for y-direction, and blue triangles for z-direction) against the actual permeability for pore-scale rock images from the Happy Spraberry formation and (b) the core-scale permeability estimated from the introduced workflow against the actual permeability for Texas Cream limestone samples.

### Step 6: Assessment of Saturation Dependent Capillary Pressure

Finally, we estimate the saturation-dependent capillary pressure curve of a core sample from Texas Cream limestone formation using the pore-throat-size distribution, calculated on Step 4, as an input to the Washburn equation (Equation 19). To compare against the results obtained from MICP measurements, we assumed the surface tension of the mercury to be 480 dynes/cm<sup>2</sup>. Figure 9 illustrates the comparison of the saturation-dependent capillary pressure of the Texas Cream limestone sample obtained from the proposed workflow against the estimates from MICP measurements.

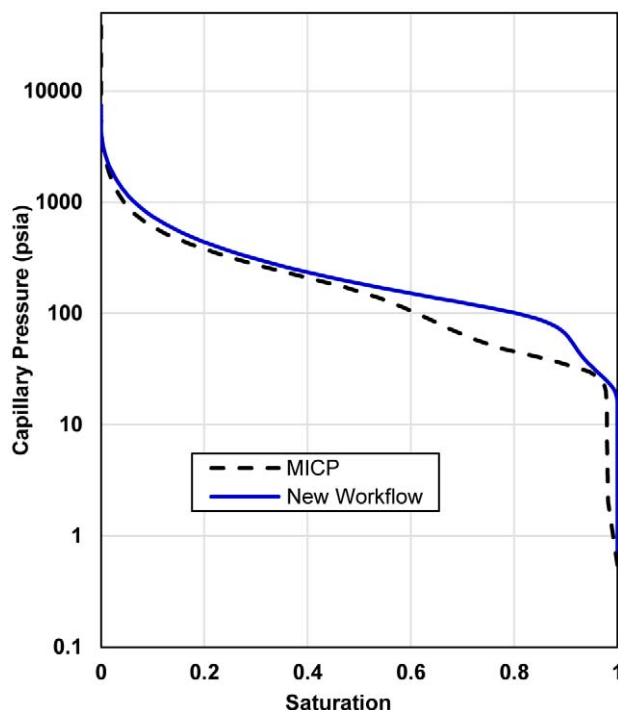


Figure 9—Comparison of the saturation-dependent capillary pressure of one Texas Cream limestone sample estimated from the proposed workflow (solid blue line) against that obtained from MICP measurements (dashed black line).

The results illustrated in Figure 9 demonstrate that the estimated saturation-dependent capillary pressure curve is in excellent agreement with the results obtained from MICP measurement for the core sample from Texas Cream limestone. Furthermore, the displacement pressure can also be reliably estimated through the new workflow.

## Conclusions

We introduced an integrated workflow that combines the interpretation of NMR, electrical resistivity, and dielectric permittivity measurements to estimate permeability tensor in formations with complex pore structures, such as carbonates, partially saturated with hydrocarbons. The new workflow also enables simultaneous estimation of constriction factor, pore- and throat-size distributions, directional permeability, and saturation-dependent capillary pressure curves. Furthermore, the equations considered in the proposed workflow are based on fundamental petrophysical principles and simplified geometries for the pore volume for the purpose of easy application to field data. Hence, all the parameters required by the workflow possess a direct physical or geometrical interpretation. The results were obtained with minimum calibration efforts and without requiring detection of cutoff values. Consequently, the new integrated workflow is ready to be tested on field data, provided that all required measurements are available.

We successfully verified the reliability of the introduced workflow both in the pore- and core-scale domains using carbonate samples with diverse pore structures. The permeability estimates in the pore- and core-scale domains were compared against pore-scale numerical simulation results and core-scale permeability measurements, respectively. The average relative error in directional permeability estimates obtained by the proposed workflow for all the pore-scale samples from the Happy Spraberry formation were less than 145%, 116%, and 70%, and of 28% for the core sample from Texas Cream limestone. In the core-scale domain, we observed larger discrepancies in permeability estimates for lower values of water saturation ( $S_w < 45\%$ ). These discrepancies could be explained by uncertainties in assessment of pore-size distribution or constriction factor in partially saturated rocks. Another reason can be the increased presence

of isolated droplets of water, as the water saturation decreases, altering the relationship between resistivity and saturation.

Finally, we compared the pore-throat-size distribution and the saturation-dependent capillary pressure curve obtained from the proposed workflow for the Texas Cream limestone sample against the results obtained from MICP measurements. We verified that the estimated curves were in excellent agreement with the measurements. The differences observed between estimated and actual permeability and capillary pressure could be explained through the assumptions and simplifications adopted by the proposed workflow, such as: (1) constriction factor for all pore sizes is constant and independent on water saturation; (2) the pores can be represented by spherical shapes to calculate the surface-to-volume ratio (required to estimate pore-size distribution from the NMR  $T_2$  distribution) and to estimate the electrical tortuosity as a function of the water saturation; and (3) the electrical and hydraulic constriction factors are approximately equal and the electrical and hydraulic tortuosities are approximately equal. Moreover, the NMR fluid substitution method proposed in this paper is analytically derived based on consistent physical principles and simplifying assumptions. However, its application to formations with multi-modal pore-size distribution or cases where the hydrocarbon and water transverse relaxation times overlap can lead to uncertainties. Additionally, the assumption that all the pores are saturated with the same volume fraction of water is simplistic. Other techniques for NMR fluid substitution have been recently proposed that do not rely on this assumption (Medellin et al. 2019a, 2019b). Nevertheless, the outcomes of this paper are promising for future well-log-based applications of the introduced workflow in carbonate formations.

## Acknowledgements

The work reported in this paper was funded by the Industrial Affiliate Research Program on "Multi-Scale Rock Physics" sponsored by BP, Equinor, ExxonMobil, Occidental Petroleum, Petrobras, and Wildcat Technologies. The authors would like to thank Glen Baum and Gary Miscoe for providing core samples and assisting us in acquiring MCIP data, and Emmanuel Oyewole, who had previously taken pore-scale samples used in this paper. The authors acknowledge the Texas Advanced Computing Center (TACC) at The University of Texas at Austin for providing High Performance Computing (HPC) resources that have contributed to the research results reported in this paper. The authors would also like to thank Andres Gonzalez, Chelsea Newgord, and Yifu Han for assistance with experimental measurements.

## Acronyms

3D	=	Three-Dimensional
CPMG	=	Carr, Purcell, Meiboom and Gill
CRIM	=	Complex Refractive Index Model
CT	=	Computed Tomography
HPC	=	High Performance Computing
LBM	=	Lattice Boltzmann Method
MFIA	=	Multi-Frequency Impedance Analyzer
MICP	=	Mercury Injection Capillary Pressure
NMR	=	Nuclear Magnetic Resonance
SM	=	Statistical Mean
SNR	=	Signal-to-Noise Ratio
TACC	=	Texas Advanced Computing Center

## Nomenclature

$A$	=	Cross-sectional area, m <sup>2</sup>
$Bi$	=	Biot number

$BiNMR$	=	NMR Biot number
$C_e$	=	Electrical constriction factor
$C_H$	=	Hydraulic constriction factor
$D$	=	Molecular diffusion coefficient, $m^2/s$
$F$	=	Formation factor
$h$	=	Convective heat transfer coefficient
$h_w$	=	Water layer thickness, m
$H_{HC}$	=	Hydrogen index of the hydrocarbon phase
$j$	=	Imaginary number
$k$	=	Permeability
$k_T$	=	Thermal conductivity
$L$	=	Distance or length, m
$L'$	=	Distance between planes per pore, m
$L_c$	=	Characteristic length
$L_e$	=	Tortuous length of the capillary tubes, m
$L_e'$	=	Tortuous length between two parallel planes, m
$L_H$	=	Characteristic hydraulic length, m
$M$	=	Total transverse magnetization per unit volume, $T/m^3$
$M_w$	=	Transverse magnetization of the water-filled volume in a partially water-saturated water-wet pore, $T/m^3$
$M_{w,0}$	=	Initial transverse magnetization of the water-filled volume in a partially water-saturated water-wet pore, $T/m^3$
$M_{HC}$	=	Transverse magnetization decay of the hydrocarbon-filled volume due to bulk relaxation of hydrocarbon in a water-wet systems
$M_0$	=	Initial transverse magnetization of the pore volume, $T/m^3$
$\hat{n}$	=	Unit vector normal to the solid-fluid interface
$P_C$	=	Capillary pressure
$r$	=	Pore radius/Characteristic length
$r_H$	=	Hydraulic radius
$r_P$	=	Pore radius
$r_T$	=	Throat radius
$S$	=	Surface of the pore
$S_w$	=	Water saturation, fraction
$t$	=	Time, s
$t_0$	=	Initial time, s
$T$	=	Temperature
$T_2$	=	Transverse magnetization decay relaxation time, s
$T_{2b}$	=	Bulk relaxation time, s
$T_{2b,w}$	=	Bulk relaxation time of the pure brine/water, s
$T_{2@S_w=1}$	=	$T_2$ times of a fully water-saturated rock, s
$T_{2@S_w \neq 1}$	=	$T_2$ times of water-saturated region, s
$V$	=	Pore volume, $m^3$
$\alpha$	=	Calibration parameter related to pore-network geometry
$\beta$	=	Calibration parameter related to pore-network geometry
$\gamma$	=	Angle
$\gamma^{wave}$	=	Wave propagation
$\gamma^{ST}$	=	Surface tension of the saturating fluid

$\gamma_g^{wave}$	= Wave propagation constant on the grains
$\gamma_w^{wave}$	= Wave propagation constant on the brine
$\gamma_{HC}^{wave}$	= Wave propagation constant on the hydrocarbon
$\gamma_R^{wave}$	= Wave propagation constant of the rock
$\epsilon_g$	= Dielectric permittivity of the grain
$\epsilon_w$	= Dielectric permittivity of the brine
$\epsilon_{HC}$	= Dielectric permittivity of the hydrocarbon
$\epsilon_R$	= Dielectric permittivity of the rock
$\epsilon_0$	= Dielectric permittivity of the free space
$\epsilon^*$	= Complex dielectric permittivity
$\theta$	= Contact angle
$A$	= Parameter characteristic of the geometry of the porous medium
$\mu_0$	= Magnetic permeability of the free space, H/m
$\rho$	= Surface relaxivity
$\sigma_w$	= Electrical conductivity of the water, S/m
$\sigma_R$	= Electrical conductivity of the rock, S/m
$\tau_e$	= Electrical tortuosity
$\tau_g$	= Geometrical tortuosity
$\tau_H$	= Hydraulic tortuosity
$\nabla\Phi$	= Gradient of electric potential, V
$\phi$	= Porosity, fraction
$\phi_c$	= Connected porosity, fraction
$\omega$	= Angular frequency, rad/s

## References

- Adamson, A. W. and Gast, A. P. 1997. *Physical Chemistry of Surfaces*, sixth edition. John Wiley & Sons, Inc.
- Archie, G. E. 1942. The Electrical Resistivity Log as an Aid in Determining Some Reservoir Characteristics. *Transactions of the AIME* **146** (01): 54–62. <http://dx.doi.org/10.2118/942054-G>.
- Arns, C. H. 2004. A Comparison of Pore Size Distributions Derived by NMR and X-Ray-CT Techniques. *Physica A: Statistical Mechanics and Its Applications* **339** (1–2): 159–165. <http://dx.doi.org/10.1016/j.physa.2004.03.033>.
- Berg, C. F. 2012. Re-examining Archie's Law: Conductance Description by Tortuosity and Constriction. *Physical Review E* **86** (4): 046314. <http://dx.doi.org/10.1103/PhysRevE.86.046314>.
- Berg, C. F. 2014. Permeability Description by Characteristic Length, Tortuosity, Constriction and Porosity. *Transport in Porous Media* **103** (3): 381–400. <http://dx.doi.org/10.1007/s11242-014-0307-6>.
- Birchak, J. R., Gardner, C. G., Hipp, J. E., and Victor, J. M. 1974. High Dielectric Constant Microwave Probes for Sensing Soil Moisture. *Proceedings of the IEEE* **62** (1): 93–98. <http://dx.doi.org/10.1109/PROC.1974.9388>.
- Bitterlich, V. W. and Wobking, H. 1970. Eine Method zur Direkten Bestimmung der Sogenannten "Geometrischen Tortuosit" (A Method for the Direct Determination of Geometrical Tortuosity). *Zeitschrift Für Geophysik* **36**: 607–620.
- Chen, S. and Doolen, G. D. 1998. Lattice Boltzmann Method for Fluid Flows. *Annual Review of Fluid Mechanics* **30**: 329–364. <http://dx.doi.org/10.1146/annurev.fluid.30.1.329>.
- Chen, H. and Heidari, Z. 2014. Pore-Scale Evaluation of Dielectric Measurements in Formations with Complex Pore and Grain Structures. *Petrophysics* **55** (06): 587–597.
- Christensen, S. A., Thern, H. F., and Vejbeck, O. 2015. NMR Fluid Substitution Method for Reservoir Characterization and Drilling Optimization in Low-Porosity Chalk. Presented at the SPWLA 56th Annual Logging Symposium, Long Beach, California, USA, 18–22 July.
- Claverie, M. 2012. *Dielectric Scanner Multifrequency Dielectric Dispersion Service*. Schlumberger, Publication 13-F-0010.
- Clennell, M. B. 1997. Tortuosity: A Guide Through the Maze, in Lovell, M.A., and Harvey, P.K., Editors, *Developments in Petrophysics*. London: Geological Society, Special Publications, 122: 299–344. <http://dx.doi.org/10.1144/GSL.SP.1997.122.01.18>.



- Garcia, A. P. and Heidari, Z. 2018a. Development of a Resistivity Model That Incorporates Quantitative Directional Connectivity and Tortuosity for Enhanced Assessment of Hydrocarbon Reserves. *SPE Journal* **23** (05): 1552–1565. Paper SPE-181571. <http://dx.doi.org/10.2118/181571-PA>.
- Garcia, A. P. and Heidari, Z. 2018b. Quantifying the Influence of Rock Fabric, Composition, and Electrical Double Layer on the Broadband Dielectric Dispersion of Organic-Rich Mudrocks. Presented at the Unconventional Resources Technology Conference, Houston, Texas, 23–25 July.
- Garcia, A. P., Han, Y., and Heidari, Z. 2018a. Integrated Workflow to Estimate Permeability Through Quantification of Rock Fabric Using Joint Interpretation of Nuclear Magnetic Resonance and Electric Measurements. *Petrophysics* **59** (05): 672–693.
- Garcia, A. P., Han, Y., and Heidari, Z. 2018b. Assessment of Pore-Throat-Size Distribution and Permeability Tensor Using Geophysical Measurements. Presented at the 2018 AGU Fall Meeting, Washington, D.C., 10–14 December.
- Hizem, M., Budan, H., Deville, B. et al. 2008. Dielectric Dispersion: A New Wireline Petrophysical Measurement. Presented at the SPE Annual Technical Conference and Exhibition, Denver, Colorado, USA, 21–24 September. <http://dx.doi.org/10.2118/116130-MS>.
- Johnson, D. L., Koplik, J., and Schwartz, L. M. 1986. New Pore-Size Parameter Characterizing Transport in Porous Media. *Physical Review Letters* **57** (20): 2564. <http://dx.doi.org/10.1103/PhysRevLett.57.2564>.
- Katz, A. J., and Thompson, A. H. 1987. Prediction of Rock Electrical Conductivity from Mercury Injection Measurements. *Journal of Geophysical Research* **92** (B1): 599–607. <http://dx.doi.org/10.1029/JB092iB01p00599>.
- Kozeny, J. 1927. Über Kapillare Leitung der Wasser in Boden. *Royal Academy of Science, Vienna, Proc. Class I* **136**: 271–306.
- Medellin, D., Ravi, V. R., and Torres-Verdin, C. 2019a. Pore-Size-Dependent Fluid Substitution Method for Magnetic Resonance Measurements. *Geophysics* **84** (1): D25–D38. <http://dx.doi.org/10.1190/geo2017-0457.1>.
- Medellin, D., Ravi, V. R., and Torres-Verdin, C. 2019b. Nonlinear Mixing Law for Magnetic Resonance Transverse-Relaxation Measurements of Dispersed Mixtures. *Geophysics* **84** (1): MR1–MR11. <http://dx.doi.org/10.1190/geo2017-0342.1>.
- Minh, C. C., Jain, V., Griffiths, R., and Maggs, D. 2016. NMR T2 Fluids Substitution. Presented at the SPWLA 57th Annual Logging Symposium, Reykjavik, Iceland, 25–29 June.
- Müller-Huber, E., Börner, F., Börner, J. H., and Kulke, D. 2018. Combined Interpretation of NMR, MICP, and SIP Measurements on Mud-Dominated and Grain-Dominated Carbonate Rocks. *Journal of Applied Geophysics* **159**: 228–240. <http://dx.doi.org/10.1016/j.jappgeo.2018.08.011>.
- Nelson, P. H. 1994. Permeability-Porosity Relationships in Sedimentary Rocks. *The Log Analyst* **35** (3): 38–62.
- Newgord, C., Garcia, A. P., Rostami, A., and Heidari, Z. 2018. Improved Interpretation of Electrical Resistivity Measurements in Mixed-Wet Rocks: An Experimental Core-Scale Application and Model Verification. *Petrophysics* **59** (05): 703–718.
- Oyewole, E., Garcia, A. P., and Heidari, Z. 2016. A New Method for Assessment of Directional Permeability and Conducting Pore Network Using Electric Conductance in Porous Media. Presented at the SPWLA 57th Annual Logging Symposium, Reykjavik, Iceland, 25–29 June.
- Palabos. 2013. Geophysics: Compute the Permeability of a 3D Porous Medium. *The Palabos Software Project*. <http://www.palabos.org/documentation/tutorial/permeability.html> (accessed 2 September 2018).
- Purba, S. A., Garcia, A. P., and Heidari, Z. 2018. A New Hierarchical Method for Rock Classification Using Well-Log-Based Rock Fabric Quantification. *Petrophysics* **59** (05): 720–734.
- Rosenfeld, A. and Pfaltz, J. L. 1968. Distance Functions on Digital Pictures. *Pattern Recognition* **1** (1): 33–61. [http://dx.doi.org/10.1016/0031-3203\(68\)90013-7](http://dx.doi.org/10.1016/0031-3203(68)90013-7).
- Schindelin, J., Arganda-Carreras, I., Frise, E. et al. 2012. Fiji: An Open-Source Platform for Biological-Image Analysis. *Nature Methods* **9** (7): 676–682. <http://dx.doi.org/10.1038/nmeth.2019>.
- Senturia, S. D. and Robinson, J. D. 1970. Nuclear Spin-Lattice Relaxation of Liquids Confined in Porous Solids. *SPE Journal* **10** (03): 237–244. <http://dx.doi.org/10.2118/2870-pa>.
- Stogryn, A. 1971. Equations for Calculating the Dielectric Constant of Saline Water (Correspondence). *IEEE Transactions on Microwave Theory and Techniques* **19** (8): 733–736. <http://dx.doi.org/10.1109/tmtt.1971.1127617>.
- Talabi, O. A. 2008. *Pore-Scale Simulation of NMR Response in Porous Media*. PhD dissertation, Imperial College London, London, UK (September 2008).
- Toumelin, E., Torres-Verdin, C., Sun, B., and Dunn, K. J. 2007. Random-Walk Technique for Simulating NMR Measurements and 2D NMR Maps of Porous Media with Relaxing and Permeable Boundaries. *Journal of Magnetic Resonance* **188** (1): 83–96. <http://dx.doi.org/10.1016/j.jmr.2007.05.024>.
- Washburn, E. W. 1921. The Dynamics of Capillary Flow. *Physical Review* **17** (3): 273. <http://dx.doi.org/10.1103/PhysRev.17.273>.

---

Wyllie, M. R. J. and Spangler, M. B. 1952. Application of Electrical Resistivity Measurements to Problem of Fluid in Porous Media. *AAPG Bulletin* **36** (2): 359–403. <http://dx.doi.org/10.1306/3D934403-16B1-11D7-8645000102C1865D>.

## Appendix A

### Tortuosity Model

In general, the petrophysical interpretation of electrical resistivity measurements aims to assess the hydrocarbon saturation of the formation of interest. However, the electrical resistivity measurements are known to be affected by important rock fabric features, such as pore volume, tortuosity, and constriction factor (Berg 2012; Garcia and Heidari 2018a). Hence, if the water saturation is known or can be obtained from complementary borehole geophysical measurements, electrical resistivity can provide important insights into the rock fabric. In particular, the workflow introduced in this paper, utilizes resistivity measurements to estimate constriction factor by applying the resistivity equation introduced by Garcia and Heidari (2018a), Equation 14, which expands the applicability of Berg's (2012) equation to partially water-saturated rocks. However, one of the required inputs to Equation 14 is the electrical tortuosity,  $\tau_e$ . Garcia and Heidari (2018a) demonstrated that the electrical tortuosity is a function of the water saturation and proposed the following semi-empirical correlation

$$\tau_e = \tau_g \left[ 1 + \alpha (1 - S_w)^\beta \right], \quad (\text{A1})$$

where  $\tau_g$  is the geometrical tortuosity, and  $\alpha$  and  $\beta$  are calibration parameters that are related to the geometry of the pore network.

In order to minimize the calibration efforts required by the introduced workflow (Figure 3), in this paper we derive a new analytical expression that relates the electrical tortuosity to the water saturation based on a simplified geometry. We assume that the pore network can be represented by a set of spherical pores, connected by throats, as depicted in Figure A1. We further assume that the spherical pores are water wet and, as the water saturation increases, the thickness of the water layer coating the surface of the grains increases as well.

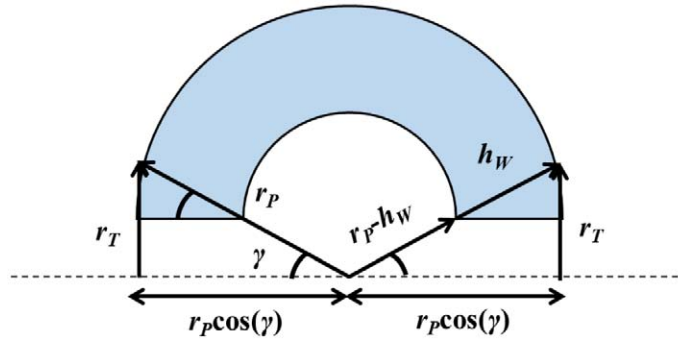


Figure A1—A cut through the synthetic pore-space model composed of spherical pore bodies partially saturated with water connected by pore throats.

The relationship between the pore radius and the throat radius is dependent on the angle  $\gamma$  via

$$\frac{r_T}{r_p} = \sin(\gamma), \quad (\text{A2})$$

by assuming that the layer of water increases without changing its shape. Moreover, if the throat size is much smaller than the pore size, we can further infer that  $\sin(\gamma) \approx \gamma$ . Hence, from Equation 9, we can establish the relationship between the angle  $\gamma$  and the constriction factor,  $C_H$ , via

$$\frac{r_T}{r_p} = \frac{1}{\sqrt{C_H}} \cong \gamma. \quad (\text{A3})$$

The electrical tortuosity can be approximated by the ratio of the length of the shortest tortuous conductive pathway between two parallel planes where the voltage difference is applied, divided by the distance between the planes (Clennell 1997; Garcia and Heidari 2018a). The distance between the planes (per pore) is equal to the minimum distance between two consecutive throats and can be calculated as

$$L' = 2r_p \cos(\gamma). \quad (\text{A4})$$

The length of the shortest tortuous conductive pathway between two parallel planes where the voltage difference is applied, on the other hand, is measured at the surface of the water film. For the simplified geometry illustrated in Figure A1, it can be calculated via

$$L_e' = 2h_w \cos(\gamma) + (\pi - 2\gamma)(r_p - h_w), \quad (\text{A5})$$

where  $h_w$  corresponds to the thickness of the water layer coating the surface of the grains. Finally, the electrical tortuosity is defined as

$$\tau_e = \tau_g \frac{L_e'}{L'}. \quad (\text{A6})$$

The geometrical tortuosity is an ad-hoc parameter that accounts for the possibility of having adjacent pores lying outside the mid-plane of the central pore. The resulting equation obtained by substituting Equations A4 and A5 into A6 is

$$\tau_e = \tau_g \left[ 1 + \left[ \frac{(\pi - 2\gamma)}{2 \cos(\gamma)} - 1 \right] \left( 1 - \frac{h_w}{r_p} \right) \right]. \quad (\text{A7})$$

However, the electrical tortuosity equation is easier to be applied to field data, if it can be directly related to the water saturation, instead of the thickness of the water layer coating the surface of the grains. In the case of simple spherical geometry depicted in Figure A1, there is a simple relationship between  $h_w$  and  $S_w$  as

$$S_w = 1 - \left( 1 - \frac{h_w}{r_p} \right)^3. \quad (\text{A8})$$

Finally, substituting Equation A8 into A7 results into the new mechanistic model relating electrical tortuosity to the water saturation via

$$\tau_e = \tau_g \left[ 1 + \left[ \frac{(\pi - 2\gamma)}{2 \cos(\gamma)} - 1 \right] (1 - S_w)^{\frac{1}{3}} \right]. \quad (\text{A9})$$

It is interesting to note that the functional form of the analytically derived Equation A9 is the same as the semi-empirical equation introduced by Garcia and Heidari (2018a) and presented in Equation A1. The main difference is that, instead of the calibration parameters  $\alpha$  and  $\beta$  from Equation A1, Equation A9 is directly related to the relevant rock fabric features of the porous media, namely the constriction factor, geometrical tortuosity, and water saturation.

## Appendix B

### NMR Interpretation and Fluid Substitution

The interpretation of Nuclear Magnetic Resonance measurements has been widely used to estimate permeability and pore-size distribution (Garcia et al. 2018a). The equations and methods for permeability assessment rely on the  $T_2$ -distribution obtained from a fully water-saturated rock. However, in real field applications, most of the measurements are performed on formations partially saturated with hydrocarbon. Consequently, a fluid-substitution algorithm is necessary to estimate the  $T_2$ -distribution of a fully water saturated rock, illustrated in Figure B1a, from the measurements performed on a partially water-saturated rock, illustrated in Figure B1b. In this appendix, we derive the basic equations necessary to perform an NMR  $T_2$  fluid substitution in water-wet sedimentary rocks.



Figure B1—Illustration of water-wet spherical pore (a) fully saturated with water and (b) partially saturated with hydrocarbon. Gray, blue, and red regions correspond to grains, water, and hydrocarbon, respectively.

The transverse magnetization decay response of a porous medium, assuming no spatial gradient of the magnetic field intensity, can be modeled by a diffusion equation with a sink term (Senturia and Robinson 1970) as

$$\frac{\partial [M]}{\partial t} = D \nabla^2 [M] - \frac{[M]}{T_{2b,w}}, \quad (\text{B1})$$

where  $[M]$  is the total transverse magnetization per unit volume ( $\text{T/m}^3$ ),  $T_{2b,w}$  is the bulk relaxation time of the water (s), and  $D$  is the molecular diffusion coefficient ( $\text{m}^2/\text{s}$ ). After the  $90^\circ$   $B_1$  pulse from the Carr, Purcell, Meiboom and Gill (CPMG) sequence at  $t = t_0$ , the initial condition is

$$[M] = [M_0] @ t = t_0. \quad (\text{B2})$$

Moreover, the boundary condition that characterizes the magnetization decay due to the interaction of the proton spins with the surface of the grains is

$$D \hat{n} \cdot \nabla [M] = \rho [M], \quad (\text{B3})$$

where  $\hat{n}$  is the unit vector normal to the solid-fluid interface.

The transverse magnetization response of a porous medium, characterized by Equations B1 to B3, is analogous to the heat conduction problem of a solid particle with an internal heat sink and boundary conditions characterized by a convective heat transfer. According to this analogy, the transverse magnetization,  $[M]$ , corresponds to the temperature,  $T$ , the surface relaxivity,  $\rho$ , corresponds to a convective heat transfer coefficient,  $h$ , and the molecular diffusion coefficient,  $D$ , corresponds to thermal conductivity,



$k_T$ , assuming a unitary heat capacity. We can also take this analogy one step further and define an NMR Biot number as

$$Bi_{NMR} \triangleq \frac{r\rho}{D}, \quad (B4)$$

where  $r$  is a characteristic length, which can be considered as the pore radius for the case of a spherical pore. The original Biot number for the heat conduction problem, analogous to the NMR problem, is

$$Bi \triangleq \frac{L_c h}{k_T}, \quad (B5)$$

where  $L_c$  is the characteristic length, which can be considered as the radius of the solid particle for a spherical particle.

The fast diffusion limit of the transverse magnetization response of a porous medium occurs when the NMR Biot number is much smaller than one (i.e.,  $Bi_{NMR} \ll 1$ ). This condition can be interpreted physically as the situation in which the diffusion process occurs much more rapidly than the relaxation at the solid-liquid interface. Analogously, in the heat conduction problem, a very small Biot number corresponds to the case in which the heat conduction within the solid occurs much more rapidly than the heat can be extracted by convection at the boundary. In other words, the temperature within the solid is approximately constant with respect to position and, consequently, the partial differential equation (thermal diffusivity equation) can be simplified to an ordinary differential equation. This simplifying approach is well known in heat conduction applications as the lumped parameter approximation. Analogously, the lumped parameter approximation can be applied to the fast diffusion limit of the NMR problem as described below.

First, we consider a control volume equal to pore containing the fluid. Then, we perform the volume integral of the NMR Diffusion Equation (Equation B1) as

$$\int_V \frac{\partial[M]}{\partial t} dV = D \int_V \nabla \cdot \nabla[M] dV - \int_V \frac{[M]}{T_{2b,w}} dV. \quad (B6)$$

In the fast diffusion limit, the transverse magnetization is approximately constant within the fluid or, equivalently, independent of position. Consequently, Equation B6 can be re-written as

$$\frac{\partial[M]}{\partial t} \int_V dV = D \nabla[M] \int_S dS - \frac{[M]}{T_{2b,w}} \int_V dV, \quad (B7)$$

where the surface integral appears from the application of Gauss' theorem to the volume integral of a divergent. Then, by applying the boundary condition to the first term on the right-hand side of Equation B7 and solving the surface and volume integrals results in the following linear first-order ordinary differential equation

$$\frac{\partial[M]}{\partial t} V = D \nabla[M] S - \frac{[M]}{T_{2b,w}} V, \quad (B8)$$

where  $S$  is the surface of the pore and  $V$  is the pore volume. The solution to Equation B8 and the initial condition, Equation B2, is

$$[M] = [M_0] \exp \left[ - \left( \frac{S}{V} \rho + \frac{1}{T_{2b,w}} \right) t \right] = [M_0] \exp \left[ - \frac{t}{T_{2@S_w=1}} \right]. \quad (B9)$$

Equation B9 describes the fast diffusion limit of the transverse magnetization response of a pore saturated with a single fluid and it is exactly the same as the equation derived by [Senturia and Robinson \(1970\)](#). Furthermore, it follows from [Equation B9](#) that the diffusion mechanisms (i.e., surface and bulk relaxation) act in "parallel" (independently) resulting in a transverse relaxation time of the pore-fluid system measured by the CPMG sequence as

$$\frac{1}{T_{2@S_w=1}} = \frac{S}{V} \rho + \frac{1}{T_{2b,w}}, \quad (\text{B10})$$

where  $T_{2@S_w=1}$  corresponds to the  $T_2$  values of a fully water-saturated rock,  $T_{2@S_w \neq 1}$  to the  $T_2$  values of water-saturated region, and  $T_{2b,w}$  to the bulk relaxation time of the pure brine.

Up to now, we made no assumption with respect to the shape of the pore. However, in order to estimate the pore-size distribution from the interpretation of NMR measurements we assume that the pores can be approximated by spheres. In such case, the surface-to-volume ratio can be calculated as

$$\frac{S}{V} = \frac{3}{r}, \quad (\text{B11})$$

where  $r$  is the pore radius. The equation that allows us to calculate the pore-size distribution can be obtained by substituting [Equation B10](#) into [Equation B11](#), resulting in

$$r_p = \frac{3\rho T_{2b,w} T_{2@S_w=1}}{T_{2b,w} - T_{2@S_w=1}}. \quad (\text{B12})$$

Next, we need to find an expression for the magnetization decay of the water-filled region of a partially saturated water-wet pore. In such case, the hydrocarbon is completely surrounded by water and, assuming that there is no spin interaction between the water and hydrocarbon, the hydrocarbon phase is only subject to the bulk relaxation. The water phase, on the other hand, is subject to both bulk and surface relaxation, but the surface relaxation only occurs at the solid-liquid interface. Hence, the surface at which the surface relaxation occurs is exactly the surface of the pore (in water-wet systems) and the ordinary differential equation that describes the fast diffusion limit of the transverse magnetization response of the water-filled volume in a partially water-saturated water-wet pore is

$$\frac{\partial[M]}{\partial t} = -\frac{4\pi r^2}{S_w \frac{4}{3}\pi r^3} [M] - \frac{[M]}{T_{2b,w}}, \quad (\text{B13})$$

where  $S_w$  corresponds to the water saturation. The solution to [Equation B13](#) is

$$[M_w] = [M_{w,0}] \exp \left[ - \left( \frac{3\rho}{S_w r} + \frac{1}{T_{2b,w}} \right) t \right] = [M_{w,0}] \exp \left[ - \frac{t}{T_{2@S_w \neq 1}} \right], \quad (\text{B14})$$

where the transverse relaxation time of the water-filled volume of the water-wet pore-fluid system measured by the CPMG sequence is

$$\frac{1}{T_{2@S_w \neq 1}} = \frac{3\rho}{S_w r} + \frac{1}{T_{2b,w}}. \quad (\text{B15})$$

Equation B14 only accounts for the contribution of the water-filled volume to the total transverse magnetization decay of two-phase fluid porous media. In reality, the total magnetization decay is a function of the water- and hydrocarbon-filled volumes as (Toumelin et al. 2007; Talabi 2008)

$$M(t) = \frac{S_w M_w(t) + H_{HC} (1 - S_w) M_{HC}(t)}{S_w + H_{HC} (1 - S_w)}, \quad (\text{B16})$$

where  $M_{HC}$  is the transverse magnetization decay of the hydrocarbon-filled volume due to bulk relaxation of hydrocarbon in a water-wet systems and  $H_{HC}$  is the hydrogen index of the hydrocarbon phase (Toumelin et al. 2007; Talabi 2008).

Most NMR measurements are performed on partially hydrocarbon-saturated rocks. Hence, in order to utilize the interpretation of NMR measurements for assessment of pore-size distribution and permeability, we need to substitute the hydrocarbon response of the original measurement (Equation B16) with an equivalent water response (Medellin et al. 2019a). In order to estimate the  $T_2$  distribution of a fully-water saturated rock from a measurement performed on a partially hydrocarbon-saturated rock, we propose a two-step NMR fluid substitution method. In the first step, we remove the NMR response due to the bulk relaxation of hydrocarbon. The second step of the NMR fluid substitution method consists on converting the  $T_2$  distribution of the water-saturated region into a  $T_2$  distribution of a fully water-saturated rock via

$$\frac{1}{T_{2@S_w=1}} = \frac{S_w}{T_{2@S_w \neq 1}} + \frac{1 - S_w}{T_{2b,w}}, \quad (\text{B17})$$

where Equation B17 can be obtained by combining Equations B10 and B15.